Novel Aspect in Grain Size Control of Nanocrystalline Diamond Film for Thin Film Waveguide Mode Resonance Sensor Application

Hak-Joo Lee,[†] Kyeong-Seok Lee,[†] Jung-Min Cho,[†,‡] Taek-Sung Lee,[†] Inho Kim,[†] Doo Seok Jeong,[†] and Wook-Seong Lee*[,†]

[†]Electronic Materials Center, Korea Institute of Science and Technology, Hwarang-ro 14-gil, Seongbuk-gu, Seoul 136-791, Republic of Korea

[‡]School of Advanced Materials Science and Engineering, Yonsei University, Seodaemun-gu, Seoul 120-749, Republic of Korea

Ⓢ *Supporting Information*

ABSTRACT: Nanocrystalline diamond (NCD) thin film growth was systematically investigated for application for the thin film waveguide mode resonance sensor. The NCD thin film was grown on the Si wafer or on the SiO_2-coated sapphire substrate using the hot filament chemical vapor deposition (HFCVD). The structural/optical properties of the samples were characterized by the high-resolution scanning electron microscopy (HRSEM), high-resolution transmission electron microscopy (HRTEM), energy dispersive X-ray spectroscopy (EDS), near edge X-ray absorption fine structure (NEXAFS), X-ray diffraction (XRD), and ultraviolet−visible (UV−vis) spectroscopy. The waveguide modes of the NCD layer were studied by prism coupler technique using laser (wavelength: 632.8 nm) with varying incident angle. A novel aspect was disclosed in the grain size dependence on the growth temperature at the relatively low methane concentration in the precursor gas, which was important for optical property: the grain size increased with decreasing growth temperature, which was contrary to the conventional knowledge prevailing in the microcrystalline diamond (MCD) domain. We have provided discussions to reconcile such observation. An optical waveguide mode resonance was demonstrated in the visible region using the microstructure-controlled transparent NCD thin film waveguide, which provided a strong potential for the waveguide mode resonance sensor applications.

KEYWORDS: *nanocrystalline diamond, grain growth, nucleation, HFCVD, waveguide mode resonance, optical property*
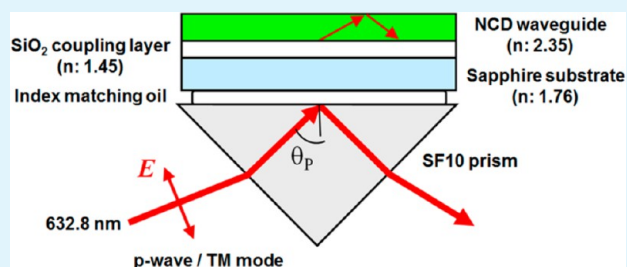
1. INTRODUCTION

Nanocrystalline diamond (NCD) and ultrananocrystalline diamond (UNCD) have been attracting strong interests for a wide variety of applications, for example, electron field emission (EFE),[1−4] nanoelectro-mechanical-system (NEMS),[5,6] implanted retinal prosthesis,[7−9] and superhard coating on stainless steel.[10] Recently, a new type of the attenuated total reflection-Fourier transform infrared (ATR-FTIR) spectroscopy was proposed.[11] It adopts an NCD thin film waveguide, coated on some optical substrates much more inexpensive than the single crystal diamond. Because the waveguide is not integrated into the main system, it could be easily separated from the main system and subjected to further surface functionalization for specific sensor applications.[11] Note that single crystal diamond is adopted as the integrated waveguide for ATR-FTIR spectroscopy;[12,13] the single crystal diamond is not only expensive but also difficult to separate from the main system for further surface functionalization to enable versatile sensor applications.

Furthermore, there is still another ATR-type optical sensor that does not rely upon the spectroscopy, which is expensive and nonportable: the waveguide mode resonance sensor equipped with a thin porous layer as the waveguide, which adopts the angular interrogation[14−21] rather than the wavelength interrogation, which requires spectroscopy.[22] Its operation relies on the waveguide modes: the standing waves generated within the waveguide layer thickness. This technique is known as an excellent optical means to study the reactions occurring in the nanoporous waveguide layer materials.[14,15,18−21] The technique has also been adopted for a label-free DNA sensing,[16] or biochemical sensing.[17] As a platform material for such bio/biochemical sensing, NCD is obviously the most promising because of its wide variety of excellent material properties.[11,23−30] However, the ATR-type optical sensor adopting porous NCD thin layer waveguide was not reported to date.

On the other hand, the excellent properties of the NCD thin film recently served as a background for some novel optical applications: the diamond-based localized surface plasmon resonance interface,[24] an electrode for the optoelectrospectroscopy,[25] and biochemical application.[27] By contrast, studies on

Table 1. Summary of the Experimental Conditions and Results

samples	substrate	CH$_4$ (%)	$T_G{}^a$ (°C)	$D_{F-S}{}^b$ (mm)	time^c (min)	grain size (nm)	thickness (nm) (R^e (nm/h))
			parameters			results	
CH$_4$ series	Si	5.0	800	10	60	5.58 (XRD)	950
		1.0	800	10	60	9.89 (XRD)	870
		0.5	800	10	60	11.91 (XRD), 18.15 (SEM)	830
T$_1$ series	Si	5.0	700	10	60	5.99 (XRD)	410
		5.0	800	10	60	5.58 (XRD)	950
		5.0	900	10	60	^{d} G	G
T$_2$ series	Si	0.5	700	40	60	15.72 (XRD), 37.54 (SEM)	130
		0.5	800	40	60	10.89 (XRD), 17.74 (SEM)	450
		0.5	900	40	60	8.97 (XRD)	800
T$_3$ series	Si	0.5	700	10	60	16.53 (XRD), 43.12 (SEM)	310
		0.5	800	10	60	11.91 (XRD), 18.15 (SEM)	830
		0.5	900	10	60	8.36 (XRD)	1010
D$_1$ series	Si	0.5	800	10	60	11.91 (XRD), 18.15 (SEM)	830
		0.5	800	20	60	11.67 (XRD), 17.92 (SEM)	730
		0.5	800	30	60	11.22 (XRD), 17.80 (SEM)	590
		0.5	800	40	60	10.89 (XRD), 17.74 (SEM)	450
D$_2$ series	Si	5.0	800	10	60	5.58 (XRD)	950
		5.0	800	20	60	6.43 (XRD)	830
		5.0	800	30	60	6.85 (XRD)	690
		5.0	800	40	60	7.14 (XRD)	520
sample A	SiO$_2$-coated sapphire	5.0	800	10	10	<10 (XRD/TEM)	100 (600)
sample B		0.5	800	40	110	50−60 (SEM/TEM)	250 (140)
sample C		0.5	700	40	190	80−90 (SEM/TEM)	220 (70)

^{a}Growth temperature (T_G). ^{b}Distance from filament to substrate (D_{F-S}). ^{c}Deposition time (time). ^{d}Graphite deposition (G). ^{e}Growth rate (R).

the angular-interrogated NCD thin film waveguide mode resonance sensor is just beginning.[31,32]

Some of the important requirements of the diamond thin film for such waveguide application might be the (1) optical transparency; (2) optical smoothness of the surface; (3) compatibility with respect to the underlying substrate material; (4) optically flawless interface between the diamond waveguide layer and the underlying substrate.

Requirement 1 would favor the minimal grain boundary area (which is usually defective) and consequently the large grains (compare ultraviolet−visible (UV−vis) transmissions of NCD and UNCD films in Table 2 of ref 33). By contrast, requirement 2 would favor small grains to minimize the surface roughness of the as-grown surface (see Table 1 in ref 34). Consequently, the optimization requires a trade-off between the two opposing requirements. Requirement 3 would favor the low growth temperature to avoid the thermal damage of the substrate. It further complicates the optimization protocol, because the vapor-grown diamond nucleation/growth is obviously sensitive to the substrate temperature. Requirement 4 demands defect/void-free high-density initial nucleation at the interface, which is often difficult to achieve on the optical substrate material such as SiO$_2$.[35] The surface pretreatment by scratching technique[36] is inadequate in this context, because it might introduce mechanical defect to the substrate surface.

For most of the aforementioned requirements, the grain size control is the key issue. It is rather straightforward for microcrystalline diamond (MCD) film since its microstructural evolution occurs in the van der Drift mode[37−39] with columnar structure (see Figure 4c in ref 39). In such a mode, the average grain size simply increases with the film thickness, in proportion to the growth time; at a given growth time, the grain size would be proportional to the growth temperature (see Figure 3d in ref 40), because it is well-known that the growth is thermally

accelerated (see Figure 2 in ref 41). Such conventional perspectives concerning the effect of growth temperature on the grain size had been extended even to the transparent NCD film synthesis. For example, Chen et al.[42] argued that "*increased substrate temperature facilitated growth of larger crystallites*" (see the discussion concerning Figure 3 in ref 42).

By contrast, the growth of UNCD film and that of some NCD film might deviate from such conventional perspectives, either because the active renucleation persists throughout the growth stage,[43] or because the relevant parameter space was extended beyond that of the conventional MCD film synthesis.[40,43] In this context, it is worth noting that May et al.[44,45] predicted a novel effect of the growth temperature on the grain size: the grain size would decrease with growth temperature (see Figure 7 in ref 44) based on their computational growth chemistry modeling. It is contrary to the aforementioned conventional perspectives held for the MCD domain, as well as to the report by Chen et al.[42] in the NCD domain. Thus, the effect of growth temperature on the grain size in the NCD domain still requires further clarification.

There are many reports on the formation of the transparent NCD layers on foreign/optical substrates.[25,27,34,42,46−57] The effects of some parameters are rather well clarified. For example, the relatively low methane concentration below 0.5% was favored for low-temperature growth of high-quality NCD in hydrogen-rich chemistry;[33] the lower pressure favored the synthesis of NCD rather than MCD.[34] To the contrary, investigations on the relationship between grain size and growth temperature is far from satisfactory in the NCD domain where the relevant parameter space substantially differs from that of the MCD domain.[34,55,58−61] In the present study, we have systematically investigated microstructural evolution in the NCD thin film during the hot filament chemical vapor deposition (HFCVD) to clarify such ambiguity, with the

11632

dx.doi.org/10.1021/am403066k | ACS Appl. Mater. Interfaces 2013, 5, 11631−11640

intention of applying it as the thin film waveguide mode resonance sensor.

2. EXPERIMENTAL SECTION

The NCD films were synthesized on the Si wafer (grade, prime; diameter, 4 in.; p-type; orientation, (100); thickness, 0.5 mm; and one-side polished) or on the sapphire wafer (grade, prime; diameter, 2 in.; refractive index, 1.76; orientation, (0001); thickness, 0.4 mm; and double-side polished) using the HFCVD technique. The sapphire substrate was precoated with 500 nm thick SiO_2 film by the radio frequency (RF) magnetron sputtering (RF power, 80 W; working pressure, 5 mTorr) as a low-index coupling layer (refractive index, 1.45), on the side where the NCD layer was to be coated. The substrate was ultrasonically seeded with nano diamond powder seeding suspension (see ref 35 for further detail). No substrate pretreatments were done to the substrate prior to seeding.

Four different series of experiments were carried out for the optimization of the microstructure (see Table 1), from which three different synthesis conditions were selected for the optical characterization (see samples A, B, and C at the last row in Table 1). The chamber pressure, precursor gas composition, and filament temperature were maintained at 7.5 Torr, 0.5−5% CH_4 in H_2, and 2100 ± 20 °C, respectively. The growth temperature (T_G) and the filament−substrate distance (D_{F-S}) were controlled in the ranges of 700−900 °C and 10−40 mm, respectively. The growth temperature was measured by thermocouple at the substrate surface; it was controlled exclusively, with other growth parameters kept unchanged, by varying the thermal contact between the substrate and the underlying water-cooled substrate holder.

The structure and grain size of the synthesized NCD films were analyzed by the high-resolution scanning electron microscopy (HRSEM, FEI Nova 200 NanoSEM), high-resolution transmission electron microscopy (HRTEM, FEI TECNAI G2 F20), energy-dispersive X-ray spectroscopy (EDS, FEI), near edge X-ray absorption fine structure (NEXAFS, at the resolution of 0.1 eV, total electron yield mode, at the 10D1 KIST beamline of the Pohang Accelerator Laboratory in Korea), and X-ray diffraction (XRD, Rigaku D/MAX-2500 using Cu Kα (λ = 0.154 nm) radiation at 40 kV and 200 mA in the range of 30−95° by step scanning with a step size of 0.02°, along with the Scherrer formula[62] using the dimensionless constant (K = 0.89) and the degree of diamond (111) peak (43.9°) to determine the grain size; Note that such approach is allowed for grain size below 100 nm).[63] The TEM samples were prepared by the focused ion beam (FIB, FEI Nova 600). The optical properties of the samples were studied by UV−vis spectroscopy (Perkin-Elmer, Lambda 35) in the 250−1100 nm wavelength range; the optical absorption coefficient (α) was determined from the measured reflectance (R) and transmittance (T). The refractive index (n) and extinction coefficient (k) were also derived by a theoretical fitting to the experimental spectra using the O'Leary−Johnson−Lim model.[64] The wave-guiding properties of the NCD layer were studied by prism coupler technique; the guided modes for p- and s-wave were characterized with varying incident angle using 632.8 nm laser.

3. RESULTS AND DISCUSSION

Table 1 summarizes the parameters and results of the present experiments. Figures 1 and 2 show the surface microstructures of the CH_4 series and those of the T_1, T_2, and T_3 series. In the CH_4 series, the grain size drastically increased with decreasing methane concentration from 5 to 0.5% (see Figure 1a−c and first row in Table 1). Such a tendency is easily understood in terms of the nucleation rate increasing with supersaturation (see Section 1.7 of ref 65).[39,44,45] By contrast, in the T_1 series with the high methane concentration of 5%, the grain size did not change with the temperature increase from 700 to 800 °C, whereas graphite was formed at 900 °C (see Figure 1d−f and second row in Table 1) as confirmed by the NEXAFS and
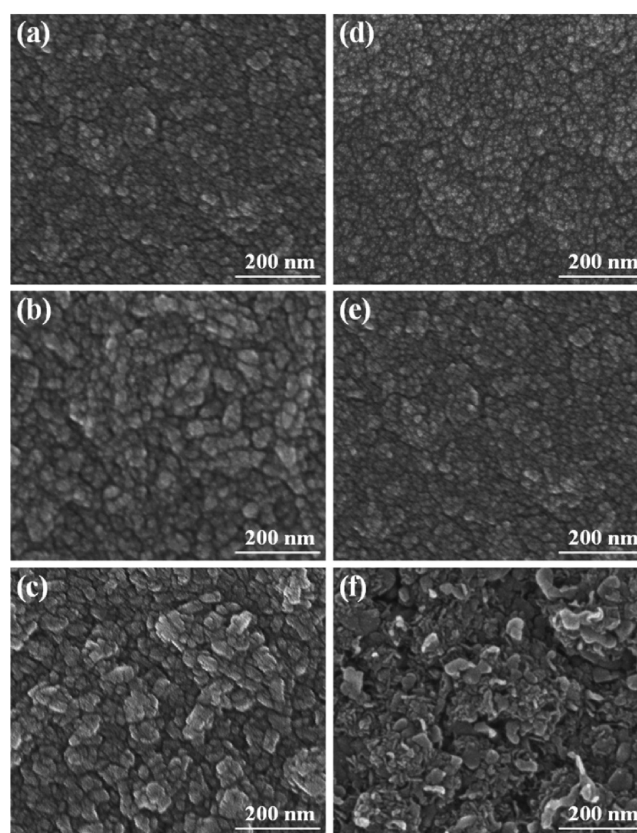

Figure 1. HRSEM image of the CH_4 series (CH_4 concentration, (a) 5, (b) 1, and (c) 0.5%) and T_1 series (T_G, (d) 700, (e) 800, and (f) 900 °C).

TEM (not shown here). Such insensitivity of the grain size to the growth temperature in the T_1 series was in a sharp contrast to the usual tendency in MCD domain where the grain size is a sensitive function of the growth temperature (see section 1; see also Figure 3d of ref 40). Moreover, the grain size even decreased drastically with the growth temperature in the T_2 series as well as in the T_3 series with the low methane concentration of 0.5% (see Figure 2, third row and fourth row in Table 1), regardless of the D_{F-S}, which was opposite to the general tendency in MCD domain. It should be attributed to the differing nucleation/growth mechanisms in the NCD and the MCD domain, which should be addressed further below.

Recall that the grain size is determined by the continued renucleation during growth in the NCD/UNCD domain.[33,43,44,66] Note that the classical nucleation theory predicts that the driving force for nucleation rate increases with supersaturation (see section 1.7 of ref 65) or, equivalently, with supercooling (see chapter IX of ref 67),[68] the grain size should decrease accordingly. For the present HFCVD environment, it is reasonable to assume that the supercooling of the growth species around the substrate is proportional to the temperature difference between the heated filament (where the growth species is generated through the thermal dissociation of the precursor gas) and the underlying cooled substrate onto which the growth species arrive to participate in the nucleation process (see section 2 for respective temperatures). With this background, the nucleation rate can be expressed as follows.[65,67,68]
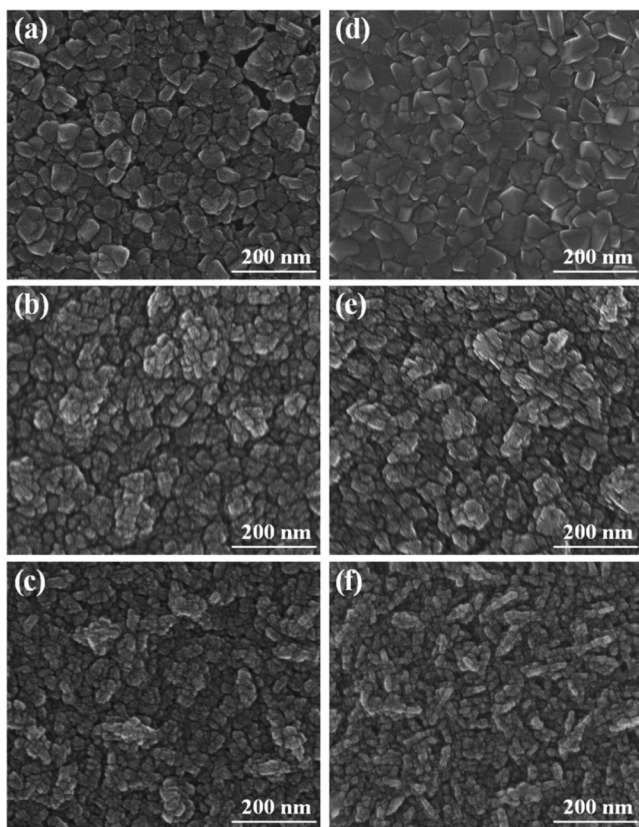
Figure 2. HRSEM image of T_2 series (D_{F-S}, 40 mm; T_G, (a) 700, (b) 800, and (c) 900 °C) and T_3 series (D_{F-S}, 10 mm; T_G, (d) 700, (e) 800, and (f) 900 °C).

Figure 3. Schematic diagram showing the effects of temperature and supercooling on the equilibrium nucleation rate and grain size.

$$\dot{N} \propto \exp\left(-\frac{\Delta G^*}{kT}\right)\exp\left(-\frac{\Delta E_D}{kT}\right) \tag{1}$$

$$\Delta G^* = \frac{16\pi\gamma^3}{3(\Delta E_V^2)}\frac{T_E^2}{(T_E - T)^2} \tag{2}$$

where $\dot{N}$ = nucleation rate, ΔG^* = energy barrier, k = Boltzmann constant, T = substrate temperature, ΔE_D = activation energy for diffusion, γ = surface free energy per unit area, ΔE_V = activation energy per unit volume, and T_E = equilibrium transformation temperature.

According to eqs 1 and 2, the supercooling would decrease with substrate temperature. The nucleation rate on the growth front is also dependent on the diffusion rate of the growth species from their source to the sink, i.e., the nucleation site on the substrate. The growth species transfer might occur through the diffusion in the gas phase from filament to substrate and consequently by surface diffusion on the substrate. The diffusion rates in both diffusion paths should exponentially increase with the temperature (see Section IX-2 of ref 67), as opposed to the aforementioned temperature dependence of the driving force for the nucleation: the diffusion rate should exponentially freeze out as the substrate temperature drops. It is well-known that such two opposing factors make a trade-off to yield a maximum at an intermediate temperature (let us name it as the threshold temperature) in the nucleation rate–temperature profile (see Figure 3 for its schematic representation); the grain size curve should show a minimum at the threshold temperature accordingly.
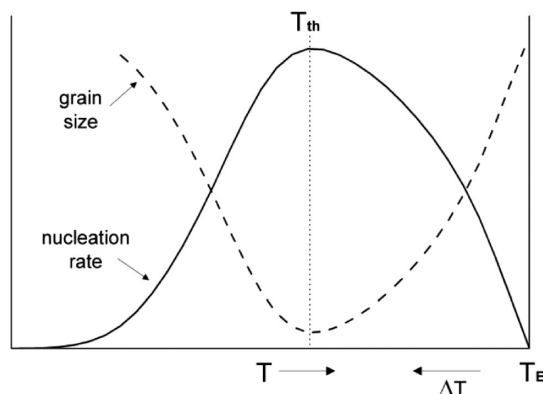
If one could assume that the substrate temperatures for the T_2 and T_3 series belonged to the temperature domain below the threshold temperature, the grain size would increase as the temperature decreased. In this context, the unexpected grain size variation in the T_2 and T_3 series (see Figure 2, third row and fourth row in Table 1) might be reconciled with such classical nucleation theory.[67,68] Nevertheless, one could not exclude the other possibility that the present substrate temperature range belonged to the temperature domain above the threshold temperature.

Note that the D_{F-S} was 40 mm in the T_2 series, as opposed to the 10 mm in the T_3 series; also note that the methane concentration was 0.5% in the T_2 series as opposed to 5% in the T_1 series (see Table 1). The grain size of the T_1 series was much less sensitive to the substrate temperature, relative to that of the T_2 or T_3 series (see Table 1). It was obviously attributed to the two differing parameters among them, i.e., the methane concentration and the D_{F-S}. It is well-known that growth species concentration, and hence the supersaturation, sharply drops (1) with D_{F-S} in HFCVD environment[45] and (2) with decreasing methane concentration in the precursor gas mixture. It follows that the supersaturation at the substrate surface in the T_1 series should have been much higher than that of T_2 series. The nucleation rate is a sensitive function of the supersaturation, in addition to that of the growth temperature.[65,67,68] Therefore, the relative importance of the growth temperature in determining the nucleation rate might have substantially weakened at the T_1 series, relative to the T_2 or T_3 series. Note that, in the CH_4 series, which was conducted at the D_{F-S} of 10 mm (see Table 1), the grain size was also relatively insensitive to the methane concentrations; it might be also understood in the same context.

On the other hand, for the D_1/D_2 series (see Figures 4 and 5 and Table 1), at first sight it was puzzling that their respective grain size variations with D_{F-S} were mutually opposite: it decreased in the former, whereas it increased in the latter. Such unexpected result could be reconciled as will be addressed below. Let us begin with the behavior of D_1 series. Recall that grain size observed at the growth surface increased with the thickness of the film having the columnar structure. Note that the NCD frequently assumes columnar structure, in contrast to UNCD, especially when grown under low methane concentration below 1%.[33] (In the present study, such columnar structure of the NCD films will be confirmed below by cross-sectional TEM observation, in relation to Figure 8). Also note that the thickness decreased with D_{F-S} in the D series (see
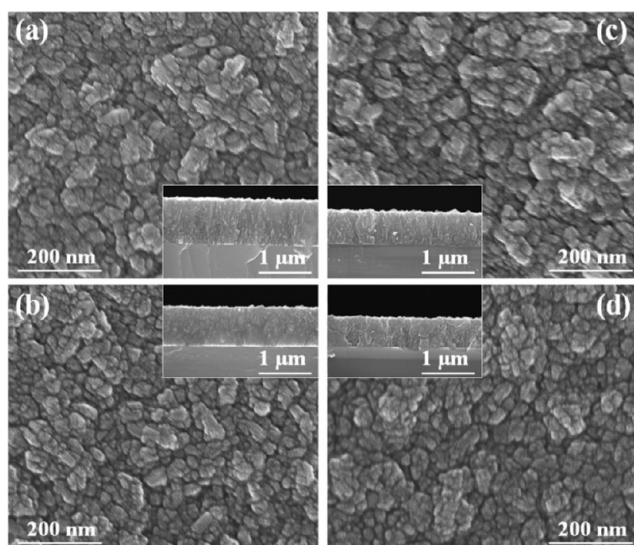
Figure 4. HRSEM image of the D_1 series (D_{F-S}, (a) 10, (b) 20, (c) 30, and (d) 40 mm; D_{F-S} = distance from filament to substrate).
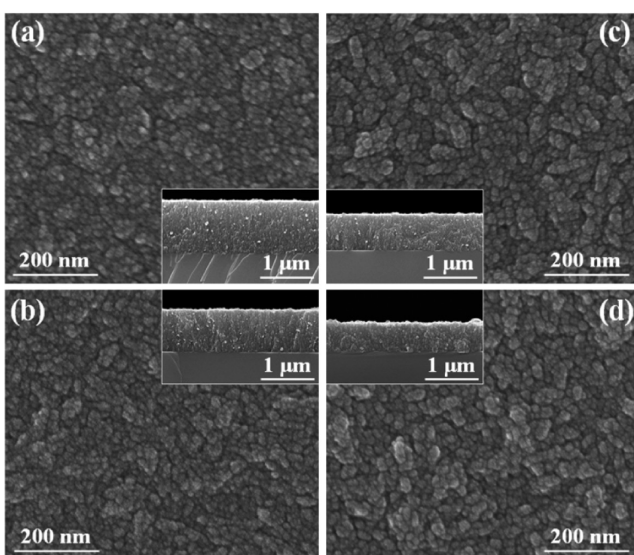

Figure 5. HRSEM image of the D_2 series (D_{F-S}, (a) 10, (b) 20, (c) 30, and (d) 40 mm; D_{F-S} = distance from filament to substrate).

insets of Figure 4 and fifth row in Table 1). The supersaturation decreasing with D_{F-S} might have resulted in the grain size increasing with D_{F-S}, because the increased D_{F-S} (see D_1 series in Table 1), through which the activated growth species should diffuse from its source (hot filaments) to the sink (substrates), might have resulted in an increased chance of their recombination; it may also result in the consequent drop in their concentration near the growth front (hence a drop in their supersaturation thereon) with the eventual drop in the nucleation rate.[69] However, the film thickness also decreased with D_{F-S} (see insets of Figure 4 and fifth row in Table 1), which was understandable because the growth rate must be also proportional to the supersaturation. The decreased thickness might have resulted in the decrease in grain size observed on the growth surface, due to its columnar structure; it might have compensated for the opposing effect of D_{F-S} on the grain size.

We should apply the same logic to the aforementioned T_2 and T_3 series. The sample thicknesses were also greater for the higher growth temperatures (see Table 1). If the effect of the columnar structure were dominant in determining the grain size at the growth surface, the grain size should have increased with the growth temperature, as opposed to the actual observation. It further confirms that the effect of the columnar structure was not the dominant factor determining the grain size of the T_2 and T_3 series, at least at relatively higher temperature range. Furthermore, comparing the grain sizes in the T_2 series against that of T_3, the greater thickness (i.e., 310, 830 nm for T_3 series vs 130 and 450 nm for T_2 series), which was attribute to the aforementioned effect of D_{F-S}, gave larger grain sizes at 700 and 800 °C, respectively. Such a tendency was attributed to the aforementioned columnar growth mode. By contrast, the opposite tendency was observed at 900 °C (see Table 1): the greater thickness (1010 nm for T_3 series vs 800 nm for T_2 series) gave smaller grain size (8.36 nm vs 8.97 nm). It indicated that the effect of the columnar growth mode, in determining the grain size, was weakened at 900 °C, probably due to the growth mode transition from the columnar to the equiaxed.

Recall that the methane concentration was as low as 0.5% in D_1 series, which must have resulted in suppressed renucleation rate, and consequently, relatively large grain size and resultant columnar growth. By contrast, the methane concentration for the D_2 series was 5%, which was ten times as high as that of D_1 series. The nucleation rate in D_s series must have been much higher accordingly, which was actually supported by the much more reduced grain size relative to that of D_1 series (see Table 1). Note that the grain size of the D_2 series was well below 10 nm. It strongly suggested that it was in the UNCD domain of which the grain structure is well-known to be equiaxed rather than columnar.[66,70] It will be further supported below by cross-sectional TEM observation (see Figure 8a). Therefore, the aforementioned effect of columnar structure, which had more than compensated the aforementioned effect of the D_{F-S} on the grain size in D_1 series, might have been absent in the D_2 series, and hence the grain size increasing with D_{F-S} in D_2 series.

Thus we have provided a qualitative set of explanations for the novel features of the grain size variation summarized in Table 1, employing the elementary classical nucleation theory with the supersaturation approach. Nevertheless, it should be noted that the present approach ignored the actually intricate steps of growth chemistry occurring in the gas phase as well as at the growth front in the vapor-growth environment, which is essential for a more quantitative analysis. In this context, an extensive analysis was reported by May et al.[44] It is important that the novel temperature dependence of the T_2 series in the present study was in accordance with their report: they predicted that the grain size increased with decreasing growth temperature (see Figure 7 in ref 44). Furthermore, the average grain size $\langle d \rangle$ in nm was given in following general form (see formula 6 in ref 44), i.e.

$$\langle d \rangle = \{2 + 0.6\exp(3430/T_s)\} \times \{[H]/[CH_3]\}^2 \qquad (3)$$

It is remarkable that the eq 3, with the calculated ratio $[H]/[CH_3]$ = 0.79 for UNCD(HF) conditions (see first column of Table 1 in ref 44), well-describes the experimental results of T_2 series with an accuracy of ~6−12%. The eq 3 correlates also with D series because of weak dependence of the near-substrate concentrations ratio $[H]/[CH_3]$ on the gap D_{F-S}. By contrast, the results of CH_4 series are less clear: the observed trend $d(CH_4)$ is predictable but the absolute variations $d(CH_4)$ were
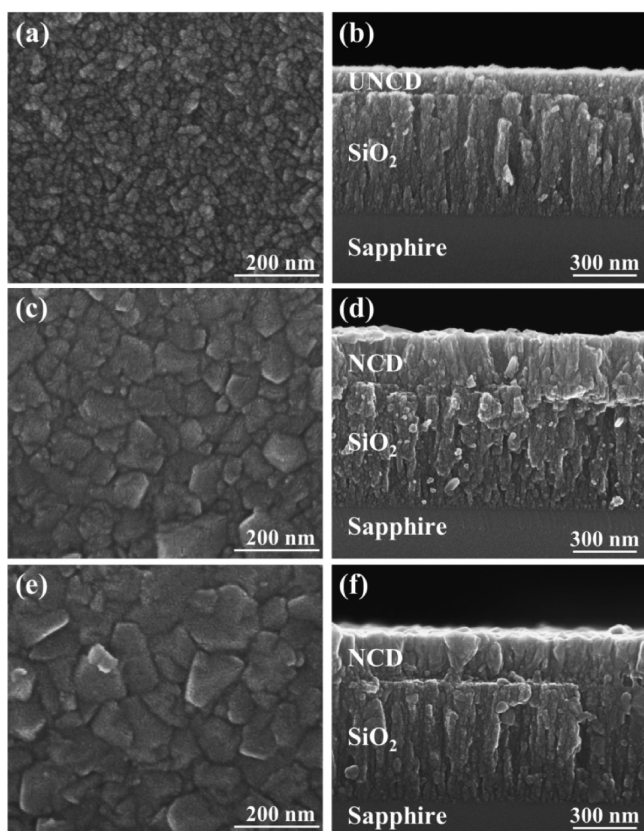
Figure 6. Plan-view and cross-sectional HRSEM images of the NCD film samples for optical characterization: (a, b) sample A, (c, d) sample B, and (e, f) sample C.

Figure 7. Photograph of the NCD film samples for optical characterizations: (a) sample A, (b) sample B, and (c) sample C.

expected to be much stronger. It should be clarified further in the future.

Based upon the observations discussed thus far, we fabricated three different diamond thin films on the SiO$_2$-coated sapphire substrate for the characterization of the optical properties, of which the experimental conditions were summarized at the last row in Table 1. The experimental parameter sets for the samples A, B, and C were chosen so that we could analyze the effect of grain size on the optical properties. We controlled the grain size into the following ranges: below 10 (UNCD), 50−60 (NCD), and 80−90 nm (NCD), respectively (see Figure 6). UNCD was chosen for comparison, whereas efforts were focused on enabling NCDs with grain sizes of tens of nanometers at a film thickness of 150−250 nm. Such grain size was chosen to suppress the grain boundary scattering, which becomes pronounced at excessive grain refining in UNCD domain. The growth temperature of 900 °C was avoided, because it gave excessive grain refining compared to 800 and 700 °C (see third row and fourth row in Table 1). The methane concentration was set to 0.5% rather than to 5%, because the latter yielded excessive grain refining, as seen from CH$_4$ series (see first row in Table 1). Another background of choosing such grain size was to suppress the scattering loss caused by surface roughness.

Figure 7 shows the visual image of the samples. The samples B and C were transparent while sample A looked rather dark, which was attributed to the excessively refined grain sizes in accordance with the previous report (see section 1).[33] Figure 8 shows the cross-sectional TEM images of the samples A, B, and C. Note that the grain size of the sample A was the finest as
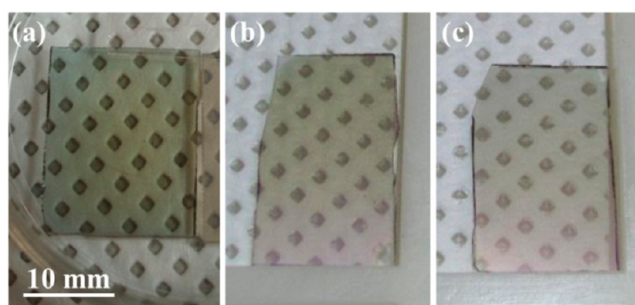
indicated above. The columnar structures were evident for the samples B and C, whereas it was not clear for the sample A. Figure 9 shows other examples of the (a) 1 μm thick UNCD, (b) 100 nm thick UNCD, (c) 100 nm thick NCD, and (d) 1 μm thick NCD film coatings on the 2 in. sapphire wafers, which compares the visual transparencies of the samples. The UNCD samples were much more opaque; it was again attributed to the excessively refined grain size.[33] The thickness dependence of the transparency was much stronger for the UNCD relative to the NCD. The excessive grain refining caused deterioration in crystallinity (see Tables S1 and S2 in the Supporting Information). It was attributed to the increased sp^2 carbon at the grain boundaries of the diamond film, as confirmed by NEXAFS and XRD analysis of the two typical samples ((a) NCD (synthesized with 0.5% CH$_4$, $T_S = 700$ °C, and $D_{F-S} = 40$ mm) and (b) UNCD (synthesized with 5.0% CH$_4$, $T_S = 800$ °C, and $D_{F-S} = 10$ mm)) (see Figures S1 and S2, Supporting Information).

Figure 10 shows the optical absorption spectra of the samples A, B, and C shown in Figure 8. The absorption coefficient (α) was obtained from the experimental transmittance (T) and reflectance (R); they were measured by the UV−vis spectroscopy, with a correction for reflectance loss at the front surface of the NCD-coated sample, i.e.

$$\alpha = \left(\frac{1}{t}\right)\ln\left[\frac{100 - R}{T}\right] \tag{4}$$

where t is the NCD film thickness. It was assumed that the contribution from the SiO$_2$-coated sapphire substrate to the total absorption was negligible. It was obvious in Figure 10 that the absorption coefficient decreased with grain size of the samples as expected (in the order of samples A, B, and C).

Figure 11 shows the refractive index and extinction coefficient of the samples. The refractive index of sample C and B were much closer to the single crystal value of 2.4, relative to that of sample A, which was much lower than that (see Figure 11a). It was also consistent with their grain sizes. The extinction coefficients showed the similar trend: it increased in the order of sample C, B, and A, which was also consistent with the order among their grain sizes (see the last row in Table 1).

The absorption coefficients, refractive index, and extinction coefficients of the samples in the present study falls well within the range of the previously reported values for diamond films synthesized by the microwave plasma chemical vapor deposition (MPCVD) or HFCVD (see Tables S1 and S2 in the Supporting Information). The value of α of sample C corresponds to the propagation length of 1.66 μm, which was not acceptable as a wave-guiding medium at visible wavelength.
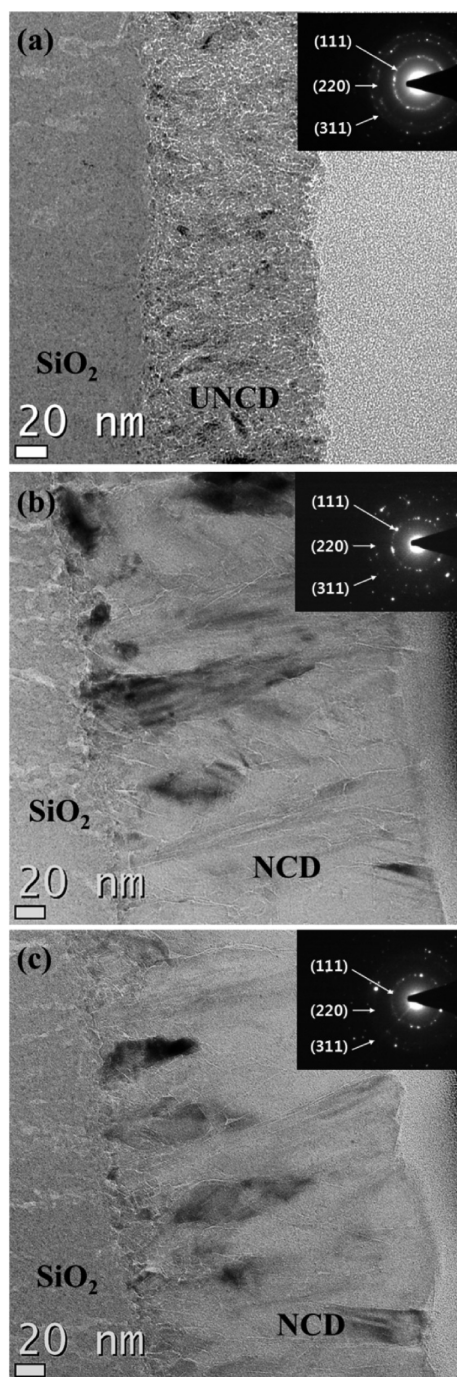
Figure 8. Cross-sectional HRTEM image of the NCD film samples for optical characterizations: (a) sample A, (b) sample B, and (c) sample C.

Figure 9. Photograph of the diamond films on the 2 in. SiO$_2$-coated sapphire wafer: (a) 1 μm thick UNCD, (b) 100 nm thick UNCD, (c) 100 nm thick NCD, and (d) 1 μm-thick NCD.

Figure 10. Optical absorption profiles of the (a) sample A, (b) sample B, and (c) sample C.

Note that the α significantly decreased with the incident wavelength as it approached IR region; it indicated that the NCD thin film waveguide is best fit for use in the infrared, rather than for the visible spectrum. However, it is important that such limitation is removed when one considers the thin film waveguide mode resonance sensor (see section 1), because it does not need any extensive light propagation along the direction parallel to the plane of the waveguide layer: its operation relies exclusively on the waveguide mode reso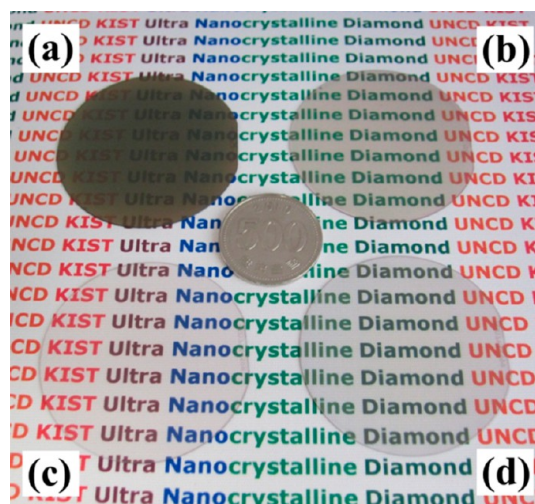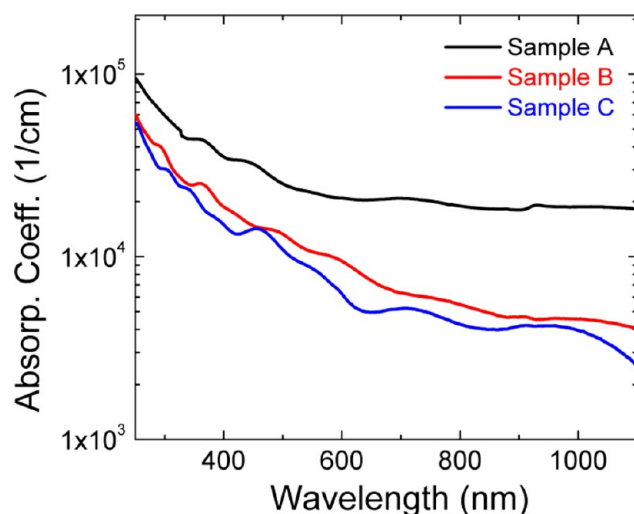nance, the standing wave generation between the two envelope surfaces of the thin film waveguide, in the direction normal to its surface (see p 238 of ref 71).[72]

For a demonstration of such waveguide modes resonance in visible region, we adopted an angular-interrogated thin film waveguide mode resonance scheme as illustrated in Scheme 1. The diamond thin films (i.e., samples A, B, and C: see Table 1), deposited on a SiO$_2$-coated sapphire substrate, were optically coupled (using an index-matching oil) to the hypotenuse plane of SF10 prism, of which the refractive index (n_p = 1.72 at 632.8 nm) was similar to that of sapphire substrate. The prism-coupled NCD thin film waveguide was then placed at the center of the high-precision two-axis rotation stage. The He/Ne laser (wavelength = 632.8 nm) was incident onto the prism base and the reflected intensity was monitored as a function of incident angle (θ_P) using a Si photodetector. A linear polarizer was used for selecting the transverse electric (TE) and transverse magnetic (TM) modes.

In general, the waveguide mode resonance exhibits a reflectance dip when the incident light transfers its energy into a guided-wave mode through the low-index SiO$_2$
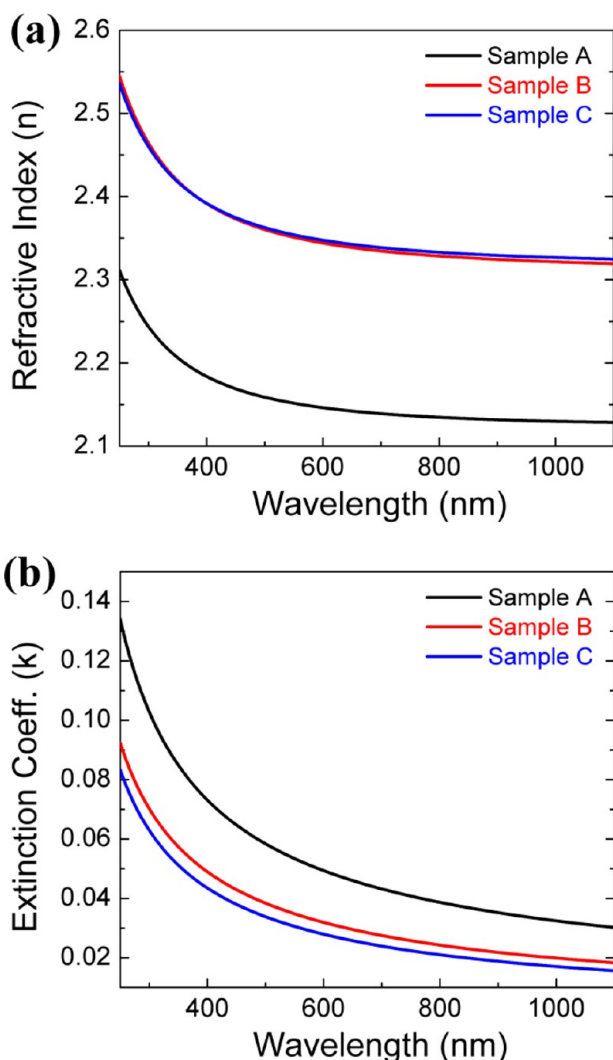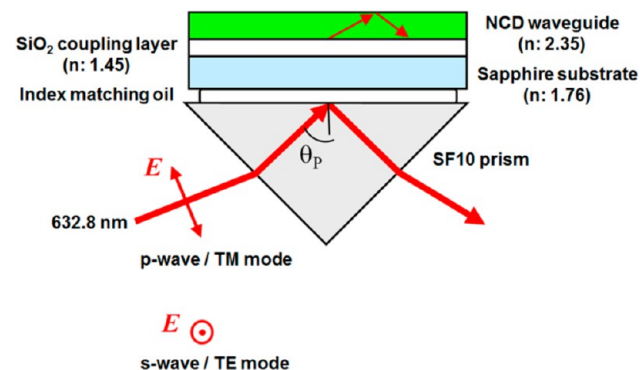
Figure 11. Optical properties ((a) refractive index and (b) extinction coefficient) of the samples A, B, and C.

Scheme 1. Schematic Diagram Showing Experimental Set up for the Waveguide Mode Detection

Figure 12. Waveguide mode ((a) TM mode (p-wave) and (b) TE mode (s-wave)) of the samples A, B, and C.

lower absorption coefficient (see Figure 12), which was also attributed to the improved optical properties of the latter, because of the optimized grain size. Note that the angular positions of the dips are sensitively shifted in response to a subtle refractive index change of the medium surrounding the waveguide.[74] Such sensitive shift could enable a novel optical sensor; relevant study is presently in progress in our group.[31] The optical transparency of the NCD thin film waveguide, which could be enabled through a careful control of the microstructure as demonstrated above, was critical in determining the depth and sharpness of the dips, and hence the sensing resolution of the sensor. Note the present study could be readily applied to the ATR sensor applications because the waveguide surface is exposed outward. This is in contrast to the recent report of Prajzler et al.,[32] where the prism-NCD/SiO$_2$/Si structure was adopted and the diamond surface was not exposed.

4. CONCLUSION

A novel aspect was disclosed in the grain size dependence on the growth temperature at the relatively low methane concentration in the precursor gas, which was important for optical property: the grain size increased with decreasing growth temperature. We have provided discussions to reconcile such observation. An optical waveguide mode resonance was demonstrated in the visible region using the microstructure-

(refractive index = 1.45) at certain phase-matching angles, during its total reflection at the prism base.[73] In the present study, the visible waveguide modes could be clearly generated in the NCD thin film waveguides, as shown in Figure 11. The relatively shallow and broad dips were evident in the sample A whose absorption coefficient was the highest. By contrast, much sharpened dips were obvious in samples B and C with much
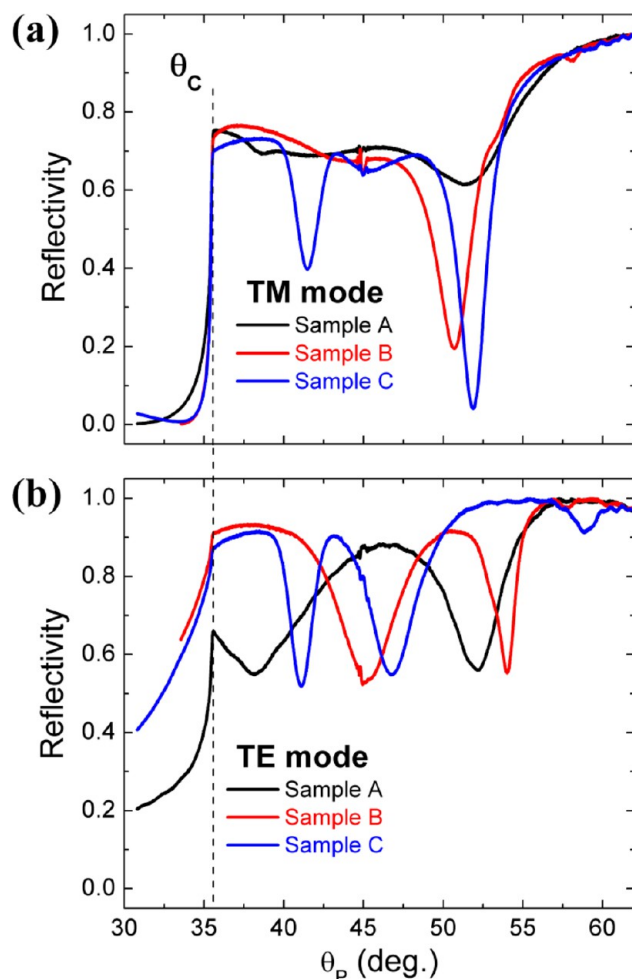
controlled transparent NCD thin film waveguide, which provided a strong potential for the waveguide mode resonance sensor applications.

ASSOCIATED CONTENT

Ⓢ Supporting Information

Tables S1 and S2 show the comparisons of diamond absorption coefficient (α); refractive index (n) and extinction coefficient (k) for the previous reports and the present results. Figures S1 and S2 provide the NEXAFS and XRD data for the NCD and UNCD films. This material is available free of charge via the Internet at http://pubs.acs.org/.

AUTHOR INFORMATION

Corresponding Author
*E-mail: wsleemk@gmail.com
Notes
The authors declare no competing financial interest.

ACKNOWLEDGMENTS

REFERENCES

(1) Pradhan, D.; Lin, I. N. *ACS Appl. Mater. Interfaces* **2009**, *1*, 1444−1450.

(2) Thomas, J. P.; Chen, H. C.; Tai, N. H.; Lin, I. N. *ACS Appl. Mater. Interfaces* **2011**, *3*, 4007−4013.

(3) Sankaran, K. J.; Panda, K.; Sundaravel, B.; Chen, H.-C.; Lin, I. N.; Lee, C.-Y.; Tai, N.-H. *ACS Appl. Mater. Interfaces* **2012**, *4*, 4169−4176.

(4) Thomas, J. P.; Chen, H.-C.; Tseng, S.-H.; Wu, H.-C.; Lee, C.-Y.; Cheng, H. F.; Tai, N.-H.; Lin, I. N. *ACS Appl. Mater. Interfaces* **2012**, *4*, 5103−5108.

(5) Sekaric, L.; Parpia, J. M.; Craighead, H. G.; Feygelson, T.; Houston, B. H.; Butler, J. E. *Appl. Phys. Lett.* **2002**, *81*, 4455−4457.

(6) Sumant, A. V.; Auciello, O.; Carpick, R. W.; Srinivasan, S.; Butler, J. E. *MRS Bull.* **2010**, *35*, 281−288.

(7) Zhou, D. D.; Greenberg, R. J. *Front. Biosci.* **2005**, *10*, 166−179.

(8) Bergonzo, P.; Bongrain, A.; Scorsone, E.; Bendali, A.; Rousseau, L.; Lissorgues, G.; Mailley, P.; Li, Y.; Kauffmann, T.; Goy, F.; Yvert, B.; Sahel, J. A.; Picaud, S. *IRBM* **2011**, *32*, 91−94.

(9) Ganesan, K.; Stacey, A.; Meffin, H.; Lichter, S.; Greferath, U.; Fletcher, E. L.; Prawer, S. *IEEE. Eng. Med. Bio.* **2010**, 6757−6760.

(10) Li, Y. S.; Tang, Y.; Yang, Q.; Maley, J.; Sammynaiken, R.; Regier, T.; Xiao, C.; Hirose, A. *Acs Appl. Mater. Interfaces* **2010**, *2*, 335−338.

(11) Osterlund L.; Andersson, P. O.; Karlesson, M; Nikolajeff, F. US 2011/0090484 A1, Apr. 21, 2011.

(12) Andersson, P. O.; Lundquist, M.; Teqler, L.; Borjejren, S.; Baltzer, L.; Osterlund, L. *ChemPhysChem* **2007**, *8*, 712−722.

(13) Andersson, P. O.; Lind, P.; Mattsson, A.; Osterlund, L. *Surf. Interface Anal.* **2008**, *40*, 623−626.

(14) Lau, K. H. A.; Tan, L. S.; Tamada, K.; Sander, M. S.; Knoll, W. *J. Phys. Chem. B* **2004**, *108*, 10812−10818.

(15) Kim, D. H.; Lau, K. H. A.; Joo, W.; Peng, J.; Jeong, U.; Hawker, C. J.; Kim, J. K.; Russell, T. P.; Knoll, W. *J. Phys. Chem. B* **2006**, *110*, 15381−15388.

(16) Rong, G. G.; Ryckman, J. D.; Mernaugh, R. L.; Weiss, S. M. *Appl. Phys. Lett.* **2008**, *93*, 161109.

(17) De Tommasi, E.; De Stefano, L.; Rea, I.; Di Sarno, V.; Rotiroti, L.; Arcari, P.; Lamberti, A.; Sanges, C.; Rendina, I. *Sensors* **2008**, *8*, 6549−6556.

(18) Cameron, P. J.; Jenkins, A. T. A.; Knoll, W.; Marken, F.; Milsom, E. V.; Williams, T. L. *J. Mater. Chem.* **2008**, *18*, 4304−4310.

(19) Yamaguchi, A.; Hotta, K.; Teramae, N. *Anal. Chem.* **2009**, *81*, 105−111.

(20) Hotta, K.; Yamaguchi, A.; Teramae, N. *Anal. Chem.* **2010**, *82*, 6066−6073.

(21) Peic, A.; Staff, D.; Risbridger, T.; Menges, B.; Peter, L. M.; Walker, A. B.; Cameron, P. J. *J. Phys. Chem. C* **2011**, *115*, 613−619.

(22) Zhang, Z.; Lu, D. F.; Qi, Z. M. *J. Phys. Chem. C* **2012**, *116*, 3342−3348.

(23) Yang, W. S.; Auciello, O.; Butler, J. E.; Cai, W.; Carlisle, J. A.; Gerbi, J.; Gruen, D. M.; Knickerbocker, T.; Lasseter, T. L.; Russell, J. N.; Smith, L. M.; Hamers, R. J. *Nat. Mater.* **2002**, *1*, 253−257.

(24) Szunerits, S.; Ghodbane, S.; Niedziolka-Jonsson, J.; Galopin, E.; Klauser, F.; Akjouj, A.; Pennec, Y.; Djafari-Rouhani, B.; Boukherroub, R.; Steinmuller-Nethl, D. *J. Phys. Chem. C* **2010**, *114*, 3346−3353.

(25) Dai, Y.; Swain, G. M.; Porter, M. D.; Zak, J. *Anal. Chem.* **2008**, *80*, 14−22.

(26) Kirste, A.; Schnakenburg, G.; Stecker, F.; Fischer, A.; Waldvogel, S. R. *Angew. Chem., Int. Ed.* **2010**, *49*, 971−975.

(27) Gao, Z.; Carabelli, V.; Carbone, E.; Colombo, E.; Demaria, F.; Dipalo, M.; Gosso, S.; Manfredotti, C.; Pasquarelli, A.; Rossi, S.; Xu, Y.; Vittone, E.; Kohn, E. *Diamond Relat. Mater.* **2010**, *19*, 1021−1026.

(28) Girard, H. A.; Perruchas, S.; Gesset, C.; Chaigneau, M.; Vieille, L.; Arnault, J. C.; Bergonzo, P.; Boilot, J. P.; Gacoin, T. *ACS Appl. Mater. Interfaces* **2009**, *1*, 2738−2746.

(29) Stehlik, S.; Izak, T.; Kromka, A.; Dolenský, B.; Havlík, M.; Rezek, B. *ACS Appl. Mater. Interfaces* **2012**, *4*, 3860−3865.

(30) Wang, X.; Ishii, Y.; Ruslinda, A. R.; Hasegawa, M.; Kawarada, H. *ACS Appl. Mater. Interfaces* **2012**, *4*, 3526−3534.

(31) Lee, K. S.; Lee, H. J.; Lee, W. S. *Int. Meet. Chem. Sens.* May 20−23; 2012; pp 1490-1491.

(32) Prajzler, V.; Varga, M.; Nekvindova, P.; Remes, Z.; Kromka, A. *Opt. Express* **2013**, *21*, 8417−8425.

(33) Butler, J. E.; Sumant, A. V. *Chem. Vap. Deposition* **2008**, *14*, 145−160.

(34) You, M. S.; Hong, F. C. N.; Jeng, Y. R.; Huang, S. M. *Diamond Relat. Mater.* **2009**, *18*, 155−159.

(35) Lee, H.-J.; Jeon, H.; Lee, W.-S. *J. Phys. Chem. C* **2012**, *116*, 9180−9188.

(36) Catledge, S. A.; Vohra, Y. K.; Mirkarimi, P. B. *J. Phys. D: Appl. Phys.* **2005**, *38*, 1410−1414.

(37) Wild, C.; Herres, N.; Koidl, P. *J. Appl. Phys.* **1990**, *68*, 973−978.

(38) Ophus, C.; Luber, E.; Mitlin, D. *Acta Mater.* **2009**, *57*, 1327−1336.

(39) Yarbrough, W. A.; Messier, R. *Science* **1990**, *247*, 688−696.

(40) Ye, H. T.; Sun, C. Q.; Hing, P. *J. Phys. D: Appl. Phys.* **2000**, *33*, L148−L152.

(41) Spitsyn, B. V. *J. Cryst. Growth* **1990**, *99*, 1162−1167.

(42) Chen, K. H.; Bhusari, D. M.; Yang, J. R.; Lin, S. T.; Wang, T. Y.; Chen, L. C. *Thin Solid Films* **1998**, *332*, 34−39.

(43) Gruen, D. M. *Annu. Rev. Mater. Sci.* **1999**, *29*, 211−259.

(44) May, P. W.; Mankelevich, Y. A. *J. Phys. Chem. C* **2008**, *112*, 12432−12441.

(45) May, P. W.; Ashfold, M. N. R.; Mankelevich, Y. A. *J. Appl. Phys.* **2007**, *101*, 053115.

(46) Stotter, J.; Zak, J.; Behier, Z.; Show, Y.; Swain, G. M. *Anal. Chem.* **2002**, *74*, 5924−5930.

(47) Mermoux, M.; Marcus, B.; Swain, G. M.; Butler, J. E. *J. Phys. Chem. B* **2002**, *106*, 10816−10827.

(48) Singh, R. K.; Gilbert, D. R.; Laveigne, J. *Appl. Phys. Lett.* **1996**, *69*, 2181−2183.

(49) Joseph, P. T.; Tai, N. H.; Chen, Y. C.; Cheng, H. F.; Lin, I. N. *Diamond Relat. Mater.* **2008**, *17*, 476−480.

(50) Remes, Z.; Izak, T.; Kromka, A.; Vanecek, M. *Diamond Relat. Mater.* **2010**, *19*, 453−456.

(51) Williams, O. A.; Nesladek, M. *Phys. Status Solidi A* **2006**, *203*, 3375−3386.

(52) Gajewski, W.; Achatz, P.; Williams, O. A.; Haenen, K.; Bustarret, E.; Stutzmann, M.; Garrido, J. A. *Phys. Rev. B* **2009**, *79*, 045206.

(53) Chen, L. C.; Kichambare, P. D.; Chen, K. H.; Wu, J. J.; Yang, J. R.; Lin, S. T. *J. Appl. Phys.* **2001**, *89*, 753−759.

(54) Remes, Z.; Kromka, A.; Vanecek, M.; Grinevich, A.; Hartmannova, H.; Kmoch, S. *Diamond Relat. Mater.* **2007**, *16*, 671−674.

(55) Kromka, A.; Rezek, B.; Remes, Z.; Michalka, M.; Ledinsky, M.; Zemek, J.; Potmesil, J.; Vanecek, M. *Chem. Vap. Deposition* **2008**, *14*, 181−186.

(56) Achatz, P.; Garrido, J. A.; Stutzmann, M.; Williams, O. A.; Gruen, D. M.; Kromka, A.; Steinmuller, D. *Appl. Phys. Lett.* **2006**, *88*, 101908.

(57) Remes, Z.; Avigal, Y.; Kalish, R.; Uzan-Saguy, C.; Chack, A.; Nesládek, M. *Phys. Status Solidi A* **2004**, *201*, 2499−2502.

(58) Griffin, J.; Ray, P. C. *Nanotechnology* **2006**, *17*, 1225−1229.

(59) Tsugawa, K.; Ishihara, M.; Kim, J.; Koga, Y.; Hasegawa, M. *J. Phys. Chem. C* **2010**, *114*, 3822−3824.

(60) Tsugawa, K.; Ishihara, M.; Kim, J.; Koga, Y.; Hasegawa, M. *Phys. Rev. B* **2010**, *82*, 125460.

(61) Xiao, X.; Birrell, J.; Gerbi, J. E.; Auciello, O.; Carlisle, J. A. *J. Appl. Phys.* **2004**, *96*, 2232−2239.

(62) Cullity, B. D. In *Elements of X-ray Diffraction*, 2nd ed.; Cohen, M., Ed.; Addison-Wesley: MA, 1978; p 102.

(63) Atta, N. F.; Galal, A.; Ali, S. M. *Int. J. Electrochem. Sci.* **2012**, *7*, 725−746.

(64) O'Leary, S. K.; Johnson, S. R.; Lim, P. K. *J. Appl. Phys.* **1997**, *82*, 3334−3340.

(65) Ohring, M. In *Material Science of Thin Films*, 1st ed.; Academic Press: New York, 1992; pp 40−43.

(66) Kulisch, W.; Popov, C. *Phys. Status Solidi A* **2006**, *203*, 203−219.

(67) Adamson, A. W. In *Physical Chemistry of Surfaces*, 5th ed.; Wiley-Interscience: New York, 1982; pp 364−378.

(68) Barrett, C. R.; Nix, W. D.; Tetelman, A. S. In *The Principles of Engineering Materials*, 1st ed.; Prince-Hall: New York, 1973; p144−192.

(69) Lee, S. T.; Lam, Y. W.; Lin, Z. D.; Chen, Y.; Chen, Q. *J. Phys. Rev. B* **1997**, *55*, 15937−15941.

(70) Konicek, A. R.; Grierson, D. S.; Gilbert, P. U. P. A.; Sawyer, W. G.; Sumant, A. V.; Carpick, R. W. *Phys. Rev. Lett.* **2008**, *100*, No. 235502.

(71) Saleh, B. E. A.; Teich, M. C. In *Guided-Wave Optics, in Fundamentals of Photonics*, 1st ed.; Goodman, J. W., Eds.; John Wiley & Sons.: New York, 1991; p 238−271.

(72) Lee, K. S.; Cho, S.; Lee, S.; Lee, T. S.; Kim, W. M. *Appl. Surf. Sci.* **2008**, *254*, 7893−7896.

(73) Lee, K. S.; Lee, T. S.; Kim, W. M.; Cho, S.; Lee, S. *Appl. Phys. Lett.* **2007**, *91*, 141905.

(74) Fujimaki, M.; Rockstuhl, C.; Wang, X.; Awazu, K.; Tominaga, J.; Fukuda, N.; Koganezawa, Y.; Ohki, Y. *Nanotechnology* **2008**, *19*, 095503.